ELSEVIER

Materials Science and Engineering A339 (2003) 81–89

MATERIALS SCIENCE & ENGINEERING A

www.elsevier.com/locate/msea

Superplasticity and grain boundary sliding characteristics in two stage deformation of Mg–3Al–1Zn alloy sheet

J.C. Tan, M.J. Tan *

School of Mechanical and Production Engineering, Nanyang Technological University, Nanyang Avenue, Singapore 639798, Singapore

Received 7 February 2002; received in revised form 7 February 2002

Abstract

A 'Two-Stage Deformation Method' was proposed to enhance the superplasticity of Mg–3Al–1Zn (AZ31) alloy sheet. This method exploited the capability of the material to undergo dynamic recrystallization (DRX) at optimum DRX conditions of 250 °C and constant strain rate of 1×10^{-4} s^{-1}. Stage I was aimed at refining the coarse microstructure of the as-received alloy to result in fine equiaxial grains measuring less than 10 μm, which deformed by grain boundary sliding accommodated by intragranular slip. Subsequently, Stage II was performed at a higher deformation temperature, whereby viscous glide mechanism accommodated by lattice diffusion was predominant. By altering the deformation mechanisms at different strain levels, elongation-to-failure of 320 and 360% was attained at 400 and 450 °C, respectively.

Keywords: Magnesium alloy; Dynamic recrystallization; Superplasticity; Grain boundary sliding; Cavitation; Viscous glide

1. Introduction

The positive effects of dynamic recrystallization (DRX) on thc superplasticity of aluminium alloys have been well documented. Some early reports by Nes [1,2] showed that as-processed Al–6Cu–0.4Zr (in wt.%) exhibited dynamic continuous recrystallization and resulted in a microstructure that can support superplastic flow during elevated temperature deformation. Microstructural evolution and superplasticity enhanced by DRX in various Al alloys such as Al–Mg alloys [3,4], Al 2219 [5], Al 7475 [6,7] and Al 6Mg–0.3Sc alloy [8] have been previously reported. However, very limited literature can be found on the effects of continuous recrystallized microstructure have on the superplasticity of hard-to-work magnesium alloys. Very recently, it was reported by Mohri et al. [9], that a Mg–9Al–1Zn alloy rolled at 673 K will undergo dynamic continuous recrystallization when deformed at 573 K and initial strain rate of 1.5×10^{-3} s^{-1}. The material which was initially of a coarse grain structure ($\approx$39.5 μm) transformed into fine grain structure ($\simeq$9.1 μm) as a result of dynamic continuous recrystallization. Subsequently, the fine-grained magnesium alloy was demonstrated to deform superplastically by grain boundary sliding (GBS), attaining an elongation-to-failure, ε_f of 604%.

DRX phenomenon of a rolled Mg–3Al–1Zn alloy sheet was previously addressed by the present authors in Part 1 [10]. The optimum DRX condition was found to be at 250 °C and at a constant strain rate of 1×10^{4} s^{-1}. During DRX, subgrains initiate in the vicinity of the serrated grain boundaries and continue to form over the whole volume of the grain through thc conversion of dislocation cell walls into subgrain boundaries. Furthermore, it was revealed that the presence of precipitates was not required for the occurrence of DRX in this material. As a result of DRX, a high volume fraction of fine ($\approx$6 μm) and equiaxial grains with large misorientation angles was attained. In the current paper, a two stage deformation method was introduced to take advantage of the fine grains produced. By identifying and altering the predominant deformation mechanism at different stages of deformation, the elongation-to-failure was improved.

* Corresponding author. Tel.: +65-790-5582; fax: +65-791-1859
E-mail address: mmjtan@ntu.edu.sg (M.J. Tan).

0921-5093/03/$ - see front matter
PII: S0921-5093(02)00097-7

2. Experimental procedures

The magnesium alloy used in this study was a commercial Mg–3Al–1Zn (AZ31B-O) cross-rolled sheet with an average grain size of 12 μm. Its chemical composition is listed in Table 1. Tensile specimens with a gauge of 15 mm length, 4 mm width and 2 mm thickness were electro-discharged machined with the tensile axis parallel to the final rolling direction.

The elevated temperature tensile tests were performed in an Instron-4206 universal testing machine equipped with electrical resistance furnace. All tests were performed in air at atmospheric pressure by employing constant strain rates. The technique of conducting elevated temperature tensile testing has been described in detail in [10]. The elongation-to-failure, ε_f, was obtained from the gauge length of the fractured specimen.

To corroborate the occurrence of GBS, specimens were polished to 0.5 μm surface finish and transverse marker lines which were oriented perpendicular to thc tensile axis were scratched onto the grains. The specimen was later deformed under the optimum DRX conditions, interrupted from the test at the specified strains and examined under the SEM. Energy Dispersive X-ray analysis (EDX) was conducted to determine the chemical composition of the filament. Specimens for optical microscopy were sectioned, cold mounted, polished and then etched in acetic picral (5 ml acetic acid +6 g picric acid+10 ml H_2O+100 ml ethanol (95%)).

3. Results and discussion

3.1. Enhanced superplasticity via two stage deformation

Rccognizing the capability of Mg–3Al–1Zn to dynamically recrystallize [10], the 'Two Stage Deformation Method' was employed to enhance superplasticity. In this method, the first stage (Stage I) of deformation was aimed at refining the coarse microstructure by utilizing the optimum DRX conditions, i.e. at 250 °C, 1×10^{-4} s^{-1} to a strain level of 60% The second stage (Stage II) was carried out at the optimum conditions that had been earlier identified [11] for superplastic deformation of a coarse-grained Mg–3Al–1Zn, i.e. 1×10^{-4} s^{-1} at 400 °C and 2×10^{-4} s^{-1} at 450 °C. Table 2 shows the results of the elevated temperature tests performed using single and two stage methods.

Although Sample 1 was deformed at optimum DRX condition and possessed a completely recrystallized microstructure, its elongation-to-failure was limited to 140% due to cavitation failure. Sample 2 was independently deformed at 400 °C and 1×10^{-4} s^{-1}, achieving 250% and a coarse-grained microstructure at fracture.

Sample 3 was tested using the two stage deformation method. It was first deformed at 250 °C, followed by a temperature increase to 400 °C at 60% strain. The strain rate remained constant at 1×10^{-4} s^{-1} throughout the test. This sample attained a total tensile elongation (i.e. sum of the first and second stages) of 320%, which was a 70% improvement over Sample 2 that was independently strained. The fractured sample is shown in Fig. 1(b) and evidently, all the samples failed by plastic necking. This implies that the recrystallized fine-grained microstructure experienced grain growth at 400 °C and consequently failed by plastic necking. Another positive effect of grain refinement was the reduction in flow stress during steady state deformation. Under the same deformation condition, the flow stress was originally at $\simeq$14.5 MPa for the single stage test; however, in the two stage test steady state flow stress was reduced to $\simeq$9 MPa, see Fig. 2(b) and (c). The reduction in flow stress was attributed to the presence of fine equiaxial grains and the involvement of different deformation mechanisms.

To further demonstrate the effectiveness of this method, Sample 5 was first deformed at the optimum DRX conditions. Subsequently, the temperature was raised to 450 °C and the constant strain rate was increased to 2×10^{-4} s^{-1}. Fig. 3(b) illustrates the results of the aforementioned deformation procedure, whilst Fig. 1(c) shows the fractured specimen. The test condition chosen for Stage II corresponded to the optimum temperature and strain rate for maximum elongation-to-failure in a single stage test, as shown in Fig. 3(a). The two stage deformation method was effective in enhancing superplasticity and concomitantly reducing the flow stress. By comparing the true stress–strain curves in Fig. 3, it is evident that ε_f was substantially improved from 265 to 360% and concurrently, thc flow stress was reduced from 9 to 6 MPa.

3.2. Grain boundary sliding characteristics

In order to explain the enhancement in superplasticity, the relevant deformation mechanisms at various stages of deformation must be taken into account. Stage

Table 1
Chemical composition (wt.%) of Mg–3Al–1Zn alloy

Mg	Al	Zn	Mn	Fe	Ni	Cu	Si	Pb	Sn	Ca
Balance	2.5–3.5	0.7–1.3	0.2 min.	0.002 max.	0.00l max.	0.002 max.	0.02 max.	0.01 max.	0.01 max.	0.002 max.

Table 2
Experimental conditions and elongation-to-failure for samples tested using single and two stage deformations

Sample number	Test temperature, °C	Strain rate, s^{-1}	Strain[a], %	Elongation-to-failure, ±5%
1	250	1×10^{-4}	–	140
2	400	1×10^{-4}	–	250
3	250 → 400	1×10^{-4}	60	320
4	450	2×10^{-4}	–	265
5	250 → 450	$1 \times 10^{-4} \rightarrow 2 \times 10^{-4}$	60	360

All samples were tested at constant strain rates.
[a] Strain where temperature or/and strain rate change occurred. The time required for raising the temperature to that of Stage II was about 10–15 min.

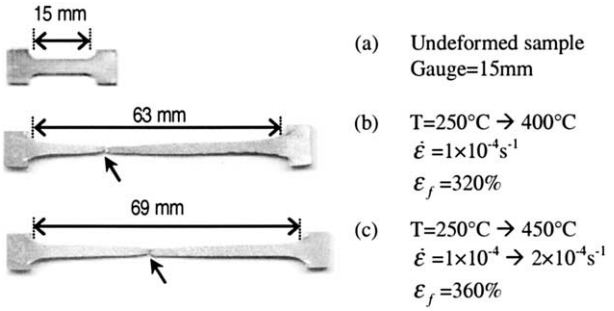

Fig. 1. Samples of the two-stage deformation tests. (a) Undeformed sample with initial gauge length of 15 mm. (b) Sample 3 failed at 320% employing Stage I: 250 °C, 1×10^{-4} s^{-1} to 60%; followed by Stage II: 400 °C, 1×10^{-4} s^{-1} till fracture. (c) Sample 5 fractured at 360% using Stage I: 250 °C, 1×10^{-4} s^{-1} to 60%; followed by Stage II: 450 °C, 2×10^{-4} s^{-1}. All samples failed by necking, as indicated by the arrows.

I which was performed at 250 °C and constant strain rate of 1×10^{-4} s^{-1} was aimed at refining the grains, hence producing homogeneous and equiaxial grains throughout the gauge of the specimen. The surface morphology of a failed specimen ($\varepsilon \simeq 140\%$) deformed at optimum DRX condition was studied under SEM to investigate the occurrence of GBS. The typical surface morphology is shown in Fig. 4, indicating significant GBS throughout the gauge region and an essentially equiaxial grain structure was retained at fracture. The retention of an equiaxial configuration even at high tensile elongation is an important criterion for superplastic materials deforming by GBS [12,13]. This is further verified by conducting a step strain rate test employing the Backofen Method [14] and the m-value was found to be $\simeq 0.5$.

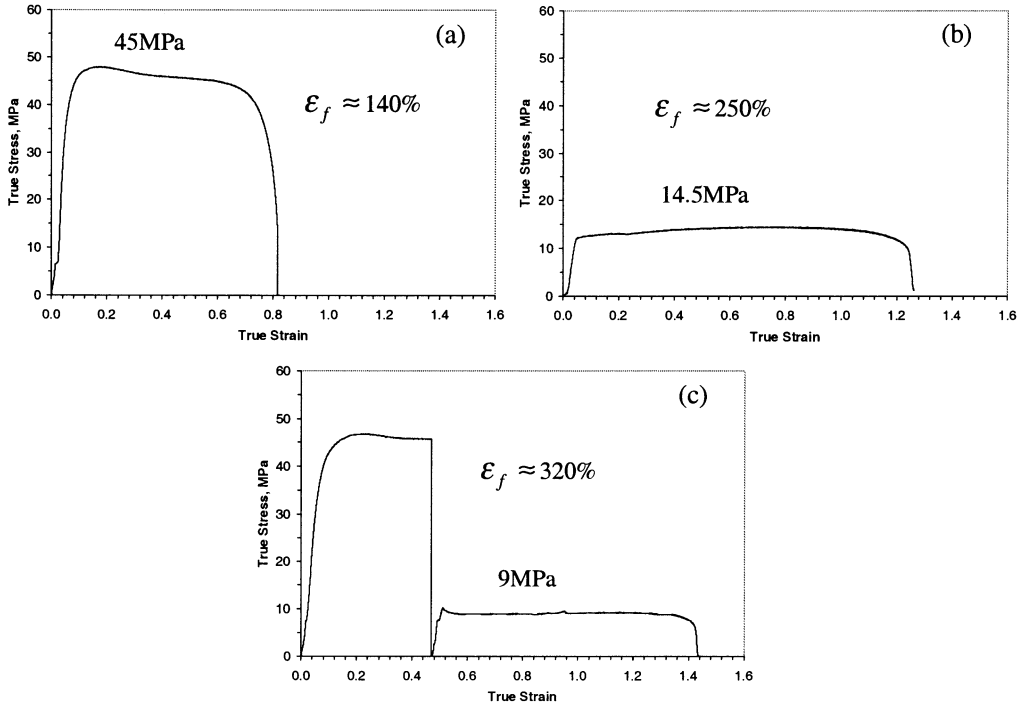

Fig. 2. True stress–strain curves showing the effects of temperature change during high temperature deformation. All tests were performed at 1×10^{-4} s^{-1} constant strain rate. Two tests were conducted independently for (a) Sample 1 at 250 °C and (b) Sample 2 at 400 °C. In (c), Sample 3 was tested using two-stage deformation at 250 °C for Stage I up to a strain of 60%, followed by Stage II at 400 °C.

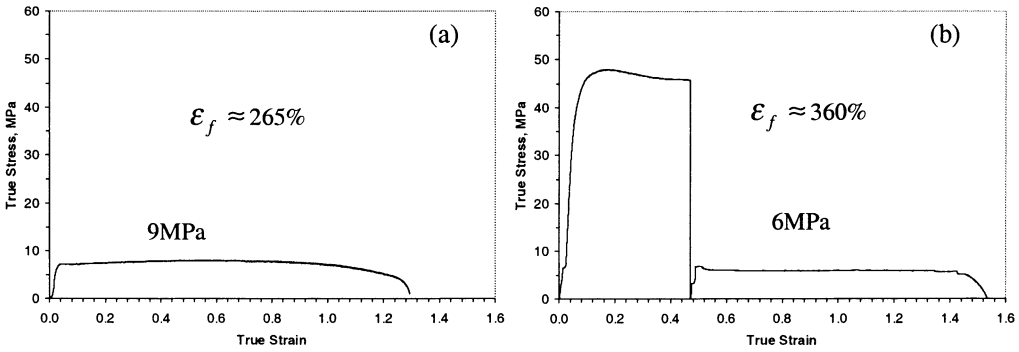

Fig. 3. True stress–strain curves showing the effects of temperature and strain rate change during high temperature deformation. (a) Sample 4 was tested at 450 °C, 2×10^{-4} s^{-1} and (b) Sample 5 was strained using two stage deformation at 250 °C, 1×10^{-4} s^{-1} for the first stage up to a strain of 60%, followed by the second stage at 450 °C, 2×10^{-4} s^{-1}. All tests were performed at constant strain rates.

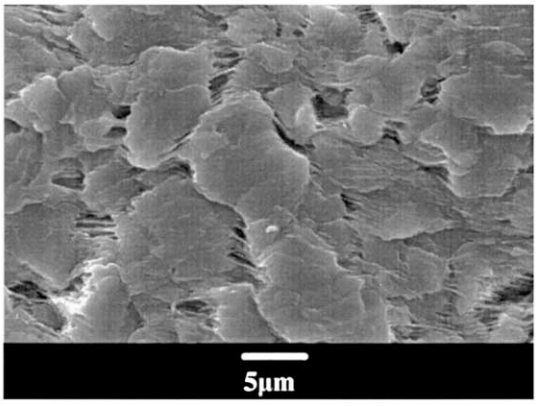

Fig. 4. The surface morphology of specimen deformed to fracture (140%) at 250 °C and 1×10^{-4} s^{-1} showing significant gain boundary sliding among the finely recrystallized grains ($\sim$6–8 μm). The tensile axis was horizontal.

To quantitatively estimate the contribution of GBS to overall strain, ξ the method for calculating ξ as proposed by Langdon [15] was employed. The strain resulted from GBS can be approximated by measuring the offset of the markers that were scratched onto the grain surface. The value of ξ can be estimated by determining the strain due to GBS, ε_{gbs}, as given by the following expression [16]:

$$\varepsilon_{gbs} = \Phi \frac{\bar{w}_l}{\bar{L}_l} \quad (1)$$

where $\bar{w}$ is thc average marker offset measured in the plane of the surface perpendicular to the tensile axis, $\bar{L}$ is the mean linear intercept grain size, Φ is a constant taken as 1.5 from creep experiments [15].The subscript l denotes that measurements are taken along a longitudinal transverse direction. The contribution of GBS to overall strain ξ is therefore given by:

$$\xi = \frac{\varepsilon_{gbs}}{\varepsilon_t} \quad (2)$$

where ε_t, is the total strain at high temperature deformation, which can be expressed by:

$$\varepsilon_t = \varepsilon_g + \varepsilon_{gbs} + \varepsilon_{dc} \quad (3)$$

where ε_g is the strain due to intragranular processes taking place within the grain and any associated accommodation process while ε_{dc} is the strain due to diffusion creep. Fig. 5 depicts the offsets of a transverse scratch mark across two grains at 60% strain and exemplifies a marker offset (w_l) measurement. A minimum of 50 measurements was collected for calculating the average offset value, $\bar{w}_l$, which was used to determine the values of ε_{gbs} and ξ.

The contribution of GBS to the total strain, ξ, is presented in Fig. 6. Measurements collected beyond the strain of 100% were inconclusive due to the ambiguous marker lines produced by excessive grain splitting and cavitation phenomena at higher strain. The values of ξ found in this work vary drastically at different strain levels. At low levels of deformation, i.e. 0–20%, the contribution of GBS was small as the coarse-grained structure (i.e. 15–25 μm) had just started to dynamically recrystallize and accordingly, GBS was not fully opera-

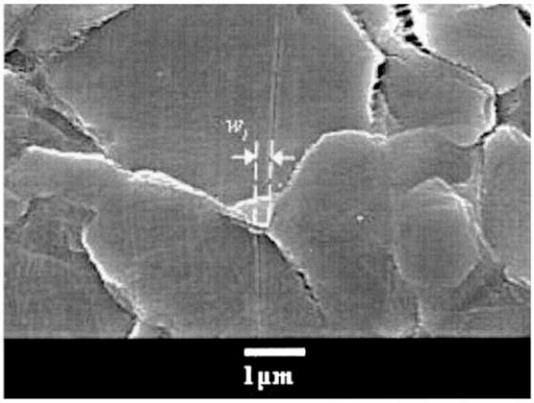

Fig. 5. The offset of a transverse marker at 60% strain, w_t the plane of the surface perpendicular to the tensile axis. The test was conducted at optimum DRX condition. The tensile axis was horizontal.

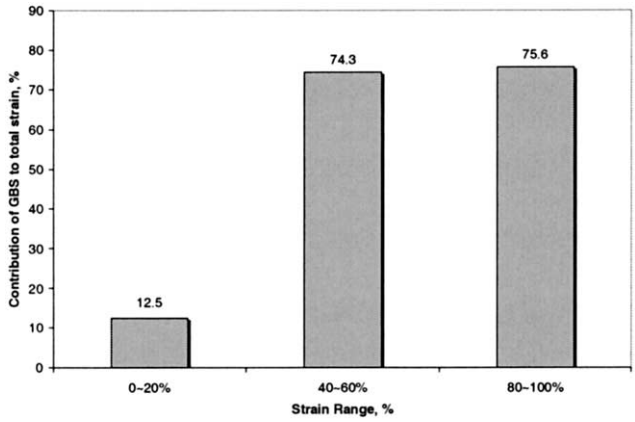

Fig. 6. Contribution of G85 to overall strain, ξ, determined at strain range of 0–20%, 40–60% and 80–100%.

tional. On the contrary, at higher strain levels, i.e. 40–60% and 80–100%, the finer grain structure (i.e. $=6$–10 μm) accounted for the high ξ which was in the range of 74–76%. The values of ξ at strain range of 40–60% and 80–100% were similar since the grain size distribution was essentially at a steady state [10]. Since the percentages of homogeneous fine grain within these strain levels were similar, their contributions towards GBS were also comparable. The calculated $\xi = 75\%$ for the fine recrystallized grains was consistent with the typical results of $\xi = 50$–70% as previously reported for other fine-grained superplastic alloys [17–20].

Even though the dynamically recrystallized grains were capable of GBS, the elongation-to-failure was relatively low, i.e. $\simeq 140\%$ using a single stage deformation at 250 °C and 1×10^{-4} s^{-1}. By examining the typical surface morphology of a fractured specimen, as shown in Fig. 7, it is evident that cavitation accounted for the premature failure. Therefore, Stage I was conducted up to only 60% and not higher in order to

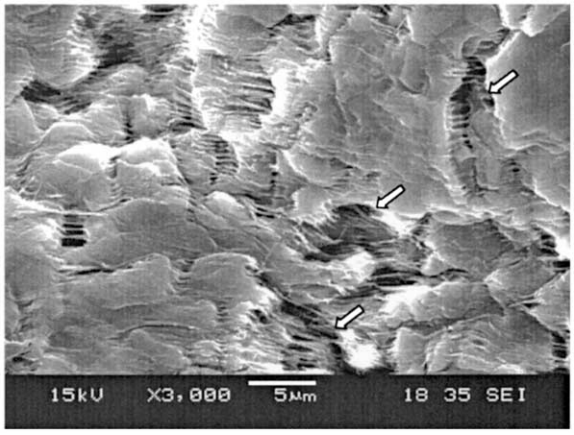

Fig. 7. SEM micrograph depicting the interlinkage of cavities. The arrows indicate the location of cavities which nucleate at grain boundaries. The specimen was strained to fracture ($\simeq 140\%$) at 250 °C and constant strain rate of 1×10^{-4} s^{-1}. The tensile axis was horizontal.

prevent the nucleation of excessive cavities which could substantially reduce the tensile elongation during Stage II.

It is well accepted that grain boundaries are potential source of weakness at elevated temperature, especially for polycrystalline materials in view of the fact that they provide nucleation sites for cavities and paths for the interlinkage of cavities which eventually leads to intergranular cracks [12]. Since the coarse-grained Mg–3Al–1Zn samples did not fail by cavitation but instead by necking, as shown in Fig. 1, the predominant deformation mechanism was viscous glide instead of GBS. Therefore, it can be concluded that fine grain size has a great impact on the nucleation of cavities in the rolled Mg–3Al–1Zn alloy.

Fig. 8(a) shows that filaments are formed between thc fine grain boundaries at the later stages of deformation, i.e. greater than 100%, when deformed under the optimum DRX condition. Relatively long filaments measuring from 2 to 5 μm were formed preferentially between the grain boundaries that were oriented more perpendicular to the stress axis, as depicted in Fig. 8(b).

Since the GBS of fine DRX grains was accommodated by intragranular slip and grain boundary diffusion, thc formation of filaments during GBS could be resulted by the high grain boundary diffusion rate of magnesium at elevated temperatures. Watanabe et al. [21] demonstrated that at 250–300 °C, a superplastic Al–6Al–1Zn magnesium alloy deformed by GBS was accommodated by slip and controlled by grain boundary diffusion. Their findings were consistent with the current alloy at the relatively low deformation temperature of 250 °C. Besides, filaments formation cannot possibly be caused by liquid phase originated from incipient melting, as has been reported by Chen and Tan [22] for a superplastic Al-7475 alloy. This is because the current deformation temperature, i.e. 250 °C was way below the reported incipient melting temperature for Mg–3Al–1Zn, i.e. 532 °C [23], therefore it was impossible for any liquid phase to form around the grain boundaries during deformation.

EDX analysis was conducted on grain 'A', grain boundary 'B' and its adjacent filament 'C', as illustrated in Fig. 9 to ascertain their chemical compositions; the results are presented in Fig. 9. Whilst Fig. 10 shows the element percentages of Al and Zn detected at points A, B and C.

Since the two major alloying elements of Mg–3Al–1Zn alloy are aluminium (2.5–3.5 wt.%) and zinc (0.7–1.3 wt.%), the major elements Mg, Al and Zn were all present at these three locations. Nevertheless, the weight percentage of Al and Zn elements was found to vary with locations. For Al element, its percentage decreased from location A to B to C. As anticipated, grain 'A' contained 2.85 wt.% of Al which was well within the 2.5–3.5 wt.% range. However, it is interesting to note

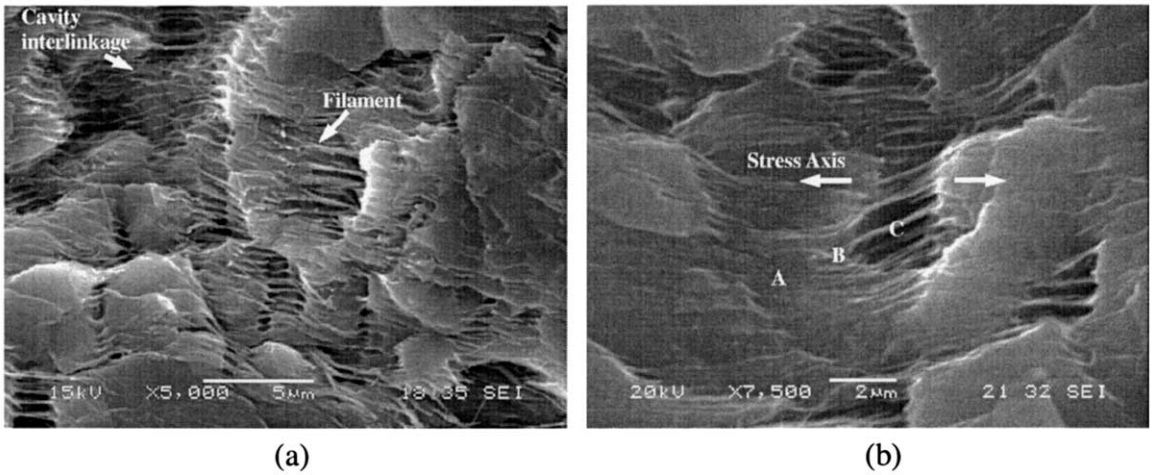

Fig. 8. Micrographs showing (a) formation of filaments between adjacent grains and cavity interlinkage (b) development of filaments an grains that are more perpendicular to the stress axis. The specimen was strained to 100% at 250 °C and constant strain rate of 1×10^{-4} s^{-1}.

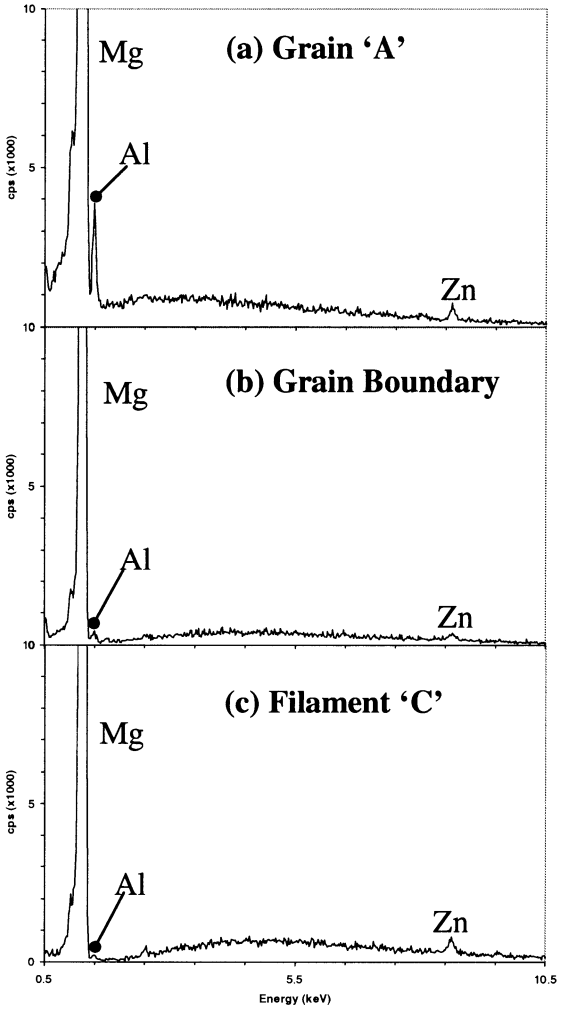

Fig. 9. EDX analyses at (a) Grain 'A' (b) Grain boundary 'B' and (c) Filament 'C', as shown in Fig. 8(b).

that the Al element at grain boundary 'B' was only 1 wt.% and was relatively close to the 0.84 wt.% found at filament 'C'. Consequently, it is reasonable to conclude that solute Al atoms did not readily diffuse into the filaments although its content was more than twice of Zn. This might be attributed to the larger atomic radius of Al as compared to Zn, i.e. 1.431 Å versus 1.332 Å, which hinders its diffusion into the magnesium host. Another possible reason is because as a result of solute atom segregation, solute Al was not found along the grain boundaries. Conversely, the percentage of Zn was similar at grain 'A' (1.28 wt.%) and filament 'C' (1.2 wt.%), while it was the lowest at grain boundary 'B' (0.58 wt.%). The above observations strongly imply that filaments formation among the DCRX grains can be ascribed to the diffusion of solute Zn atoms from the grain boundaries into the filaments, therefore rendering the grain boundaries low in Zn content. It is thereby suggested that the formation of filaments in Mg alloy is mainly driven by the diffusion of solute Zn atoms from the adjacent grain boundaries.

The schematic in Fig. 11 clearly illustrates the cavitation phenomenon in DRX grains. When the filaments between the adjacent grains are fractured, cavities are formed in between the adjacent grain boundaries. Since these cavities originate from the fractured filaments, their sizes (3–6 μm) are comparable to the length of the filaments (2–5 μm). Furthermore, attributed to the preferential nature of filaments formation, cavity nucleation is also inhomogeneous. The nucleated cavities tend to coalesce with the neighboring cavities and the interlinkage of cavities occurs easily because of the fine grain size ($\simeq$ 6–8 μm). Subsequently, interlinkage of cavities will result in intergranular cracks and fracture.

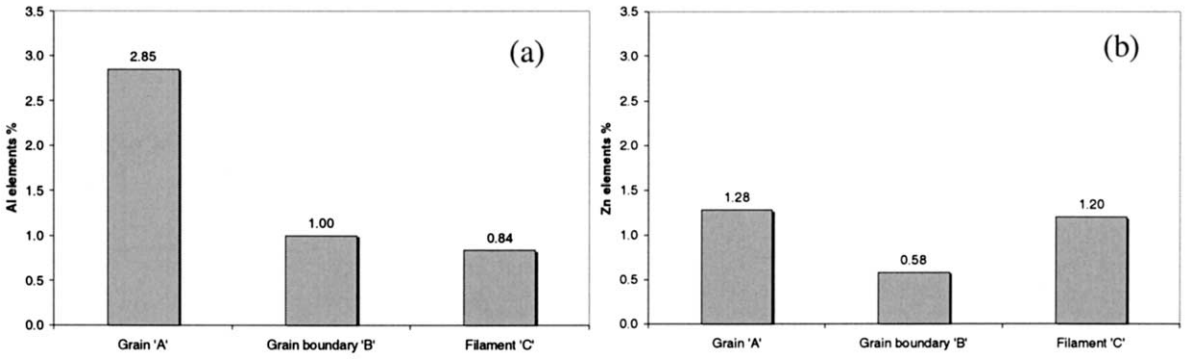

Fig. 10. Element percentages (in wt.%) of (a) Aluminium and (b) Zinc detected at points A, B and C in Fig. 8(b).

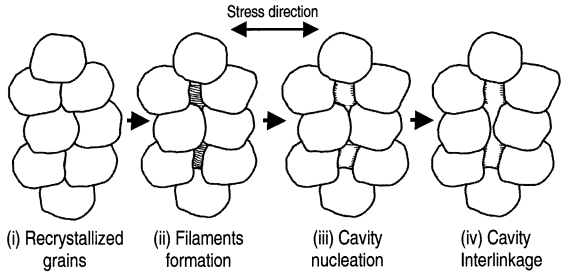

Fig. 11. Cavitation phenomenon in fine DCRX grains. (i) Fine recrystallized grains. (ii) Filaments are developed preferentially at grain boundaries that are oriented more perpendicular to the stress axis. (iii) Filaments that fracture from cavities. (iv) Interlinkage of neighboring cavities to form intergranular cracks. The stress axis is horizontal.

3.3. Summary of deformation mechanisms

At Stage II, the temperature and/or strain rate were increased to the optimum deformation conditions of coarse-grained Mg–3Al–1Zn, i.e. 1×10^{-4} s^{-1} at 400 °C or 2×10^{-4} s^{-1} at 450 °C. Attributed to the higher deformation temperature, grain growth takes place and consequently altering the predominant super-plastic deformation mechanism. As shown in Fig. 12(c), when the strain was greater than 150% in the two-stage deformation method, the coarse grain size did not permit GBS. On the contrary, viscous glide mechanism accommodated by lattice diffusion was predominant since the m-value was found to be $\simeq 0.3$ and the failure mode was necking due to the relatively low strain rate sensitivity. Detailed analysis and discussion concerning the deformation mechanisms of coarse-grained super-plastic alloys can be found in [11,24–27].

The fact that the transition from Stage I to II did not occur instantaneously suggests that a transition stage existed, hereby denoted as Stage I→II. Experimental results indicated that this stage occurred at strain level of about 100–150%. Thc microstructure present in this stage was a mixture of fine and coarse grains, as shown in Fig. 12(b). The coarser grains originated from the initially fine DRX grains, but had grown as a result of the higher deformation temperature. Step strain rate test performed within this stage found that the m-value was $\simeq 0.4$. It is interesting to note that this m-value was in between 0.3 and 0.5, inferring that the deformation mechanism could be a combination of GBS and viscous glide mechanism. This was possible since the fine grains

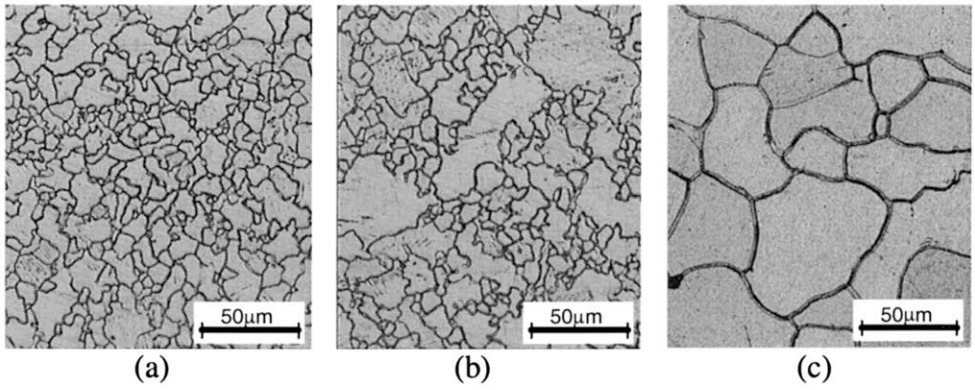

Fig. 12. Microstructural evolution and the deformation mechanism at (a) Stage I: GBS is predominant (b) Stage I→II: a combination of GBS and viscous glide mechanisms (c) Stage II: viscous glide mechanism is predominant. The elongation-to-failure was 320% and the tensile axis was horizontal.

Table 3
Summary of the related deformation mechanisms for the two stage superplastic deformation

Deformation stage	I	I → II	II
Strain level	up to 100%	> 100–150%	> 150% to failure
Average grain size	⩽ 10 μm	≃ 11–30 μm	≃ 30–100 μm
Test conditions	$T = 250$ °C, $\varepsilon = 1 \times 10^{-4}$ s^{-1}, $\varepsilon = 60\%$	Optimal superplastic conditions[a] from $\varepsilon = 60\%$ till fracture	
Microstructural condition	Fine equiaxial grains with high angle boundaries	Mixture of fine and coarse grains	Coarse grains
Deformation Mechanism	Grain boundary sliding (GBS)	GBS and viscous glide	Solute drag/viscous Glide
Accommodation process	Intragranular slip and grain boundary diffusion	Intragranular slip and diffusional flow	Lattice diffusion
m-value	≃ 0.5	≃ 0.4	≃ 0.33

[a] $T = 400$ °C, constant $\varepsilon = 1 \times 10^{-4}$ s^{-1} or $T = 450$ °C, constant $\varepsilon = 2 \times 10^{-4}$ s^{-1}.

were capable of GBS whereas the coarser grains deformed by viscous glide. This finding is also consistent with the work by Zelin et al. [28] involving the interaction of high temperature deformation mechanisms in a Mg–1.5Mn–0.3Ce (in wt.%) magnesium alloy containing a mixture of fine and coarse grains. The above discussions can be summarized in Table 3.

4. Conclusions

(1) The proposed 'Two-Stage Deformation' method is effective in enhancing the elongation-to-failure of Mg–3Al–1Zn sheet alloy. By varying thc deformation mechanisms at different strain levels, thc maximum elongation attainable at 400 and 450 °C can be improved from 250 and 265% to 320 and 360%, respectively.

(2) The first stage is carried out at the optimum DRX condition aiming at inducing DRX to produce fine equiaxial grains. Subsequently, the second stage at higher temperature is designed to take full advantage of these fine grains in order to achieve maximum elongation-to-failure.

(3) The recrystallized grains deform by GBS and its contribution towards the overall strain, ξ, was found to be ranging from 74 to 76%.

(4) The failure mode of DRX grains is via cavitation. These cavities originate from the fractured filaments and due to the preferential nature of filaments formation, cavity nucleation is inhomogeneous. The nucleated cavities tend to coalesce and interlinkage of cavities will result in intergranular cracks and fracture.

(5) In Stage I, the predominant superplastic deformation mechanism of the fine grains is GBS while in Stage II, because of grain growth, the coarser grains deform by viscous glide mechanism. The transition Stage I → II exhibits a mixture of finer and coarser grains and therefore both GBS and viscous glide deformation mechanisms could be operational.

References

[1] E. Nes, J. Mater. Sci. 13 (1978) 2052.
[2] E. Nes, J. Met. Sci. 13 (1979) 211.
[3] E.W. Lee, T.R. McNelly, Mater. Sci. Eng. 93A (1987) 45.
[4] S.J. Hales, T.R. McNelly, H.J. McQueen, Metall. Trans. 22A (1991) 1037.
[5] O.S. Sitdikov, R.O. Kaybyshev, I.M. Safarov, I.A. Mazurina, Physics Metals Metallography 92 (3) (2001) 270.
[6] X. Yang, H. Miura, T. Sakai, Mater. Sci. Forum 304 (3) (1999) 103.
[7] T. Sakai, X.Y. Yang, H. Miura, Mater. Sci. Eng. 234A (1997) 857.
[8] T.G. Nieh, L.M. Hsiung, J. Wadsworth, R. Kaibyshev, Acta Mater. 46 (8) (1998) 2789.
[9] T. Mohri, M. Mabuchi, N. Nakamura, T. Asahina, H. Iwasaki, T. Aizawa, K. Higashi, Mater. Sci. Eng. A290 (2000) 139.
[10] J.C. Tan, M.J. Tan, Dynamic continuous recrystallization characteristics in two stage deformation of Mg–3Al–1Zn alloy sheet, Mater. Sci. Eng. A, (2001) in press.
[11] J.C. Tan, M.J. Tan, Superplastic deformation behavior in Mg–3Al–1Zn alloy sheet, Mater. Sci. Eng. A, submitted for publication.
[12] T.G. Langdon, Mater. Sci. Eng. A166 (1993) 67.
[13] K.A. Padmanabhan, G.J. Davies, Superplasticity, Springer, Berlin, 1980.
[14] W.A. Backofen, I.R. Turner, D.H. Avery, ASM Trans. Quart. 57 (1964) 980.
[15] T.G. Langdon, Metall. Trans. 3 (1972) 797.
[16] R.L. Bell, C. Graeme-Barber, T.G. Langdon, Trans. AIME 239 (1967) 1821.
[17] R.Z. Valiev, O.A. Kaibyshev, Acta Metall. 31 (1983) 2121.
[18] K. Matsuki, N. Hariyama, M. Tokizawa, Y. Murakami, Met. Sci. 17 (1983) 503.
[19] T.G. Langdon, J. Mater. Sci. 16 (1981) 2613.
[20] R.C. Gifkins, Mater. Forum 15 (1991) 82.
[21] H. Watanabe, T. Mukai, M. Kohzu, S. Tanabe, K. Higashi, Acta Mater. 47 (14) (1999) 3753.
[22] C.L. Chen, M.J. Tan, Mater. Sci. Eng. A298 (2001) 235.
[23] M.A. Michael, H. Baker (Eds.), ASM Specialty Handbook: Magnesium and Magnesium Alloys, ASM International, (1999) Materials Park, OH.

[24] E.M. Taleff, D.R. Lesuer, J. Wadsworth, Metall. Mater. Trans. 27A (1996) 343.
[25] F. Li, D.H. Bae, A.K. Ghosh, Acta Mater. 45 (9) (1997) 3887.
[26] P.A. Friedman, A.K. Ghosh, Metall. Trans. 27A (1996) 3827.
[27] R. Verma, P.A. Friedman, A.K. Ghosh, S. Kim, C. Kim, Metall. Trans. 27A (1996) 1889.
[28] M.G. Zelin, H.S. Yang, R.Z. Valiev, A.K. Mukerjee, Metall. Trans. 23A (1992) 3135.